

Nanoscale

Accepted Manuscript



This is an *Accepted Manuscript*, which has been through the Royal Society of Chemistry peer review process and has been accepted for publication.

Accepted Manuscripts are published online shortly after acceptance, before technical editing, formatting and proof reading. Using this free service, authors can make their results available to the community, in citable form, before we publish the edited article. We will replace this *Accepted Manuscript* with the edited and formatted *Advance Article* as soon as it is available.

You can find more information about *Accepted Manuscripts* in the [Information for Authors](#).

Please note that technical editing may introduce minor changes to the text and/or graphics, which may alter content. The journal's standard [Terms & Conditions](#) and the [Ethical guidelines](#) still apply. In no event shall the Royal Society of Chemistry be held responsible for any errors or omissions in this *Accepted Manuscript* or any consequences arising from the use of any information it contains.

One pot aqueous synthesis of nanoporous Au₈₅Pt₁₅ material with surface bound Pt islands: An efficient methanol tolerant ORR catalyst†

Cite this: DOI: 10.1039/x0xx00000x

P. Anandha ganesh and D. Jeyakumar*

Received 00th June 2014,
Accepted 00th June 2014

DOI: 10.1039/x0xx00000x

www.rsc.org/

First time, we are reporting the synthesis of Au_{100-x}Pt_x nanoporous materials in the size range of 7-10 nm through galvanic replacement of Ag by Pt from Au_{100-x}Ag_{2x} spherical nano-alloys (x = 20, 15, 10 and 5) in aqueous medium. The galvanic replacement reaction follows 'Volmer-Weber' growth mode resulting in the formation of surface bound Pt islands on nanoporous Au surface. The high angle annular dark field image and low angle X-ray diffraction studies confirm the presence of nanoporous Au_{100-x}Pt_x NPs. The electrochemical studies using Au₈₅Pt₁₅/C catalyst show excellent methanol tolerance behaviour and better performance towards oxygen reduction reaction in terms of high mass activity, mass-specific activity and figure of merit (FOM) when compared to HiSPEC Pt/C commercial catalyst. Preliminary studies on the full cell using nanoporous Au₈₅Pt₁₅/C (loading 1.0 mg/cm²) as cathode material and Pt-Ru/C (loading 0.5 mg/cm²) as anode material performed well (38 mW cm⁻²) than HiSPEC Pt/C cathode material (16 mW cm⁻²).

Introduction

The endeavour on the development of small organics fuel cells including methanol is pursued intensively owing to the advantages like high volumetric energy density, ease of handling and storage, simple cell design, along with possible low temperature operation.¹⁻⁵ Among the small organics, methanol oxidation reaction (MOR) pathway doesn't involve complex C-C cleavage¹ and hence, work on the development of direct methanol fuel cell (DMFC) has been intense. However, the efficiency of DMFC was not fully realized due to the following reasons 1) the 'methanol cross over' from the anode side to the cathode side (through proton exchange membrane), 2) 'sluggish ORR kinetics' at cathode side and 3) the 'catalytic CO-poisoning' at anode side.² Since, Pt based catalysts are used in DMFC for both anodic MOR (Pt-Ru/C) and cathodic ORR (Pt/C), the methanol cross over results in mixed potential generation due to simultaneous ORR and MOR at cathode, which diminishes the cell voltage and current,

thereby lowering the cell performance. Thus, there is a global need for more reliable, efficient and truly methanol tolerant catalysts for ORR.

Large number of research groups are actively working on methanol tolerant ORR catalysts.⁶⁻¹³ In this regard, bimetallic nanostructures comprising Pt as one of the components with either one of Pd, Au and transition metals (Fe, Co, Ni) as the other component, with varying surface morphologies and compositions have been under consideration.^{11,12,14} It is well established that, bimetallic catalysts not only provides enhanced catalytic activity through synergistic effect,¹⁵ but also helps in minimizing the cost of its precious or less abundant metallic counterpart, in the present case Pt. Pt/Pd based bimetallic nano-alloys, core-shell nanostructures, nano-dendrites, core-porous shell structures and Pt decorated NPs were synthesized and extensively studied and the enhanced ORR activity was attributed to the lowering of 'd' band centre value.¹⁶⁻²⁵ Recently, Au-Pt core shell nanostructures have been reported with better ORR activity owing to electronic coupling effect of Au core and porous Pt shell,²³ strain effects of core metals.²⁶ The beneficial effect of Au-Pt alloying could be ascribed to the enhanced chemical activity of Pt (higher density of states) and support surface periodicity of Au providing higher turnover rates in DMFCs.²⁷ Research activities currently focus on the effect of nanostructured topography and modification of surface morphology towards ORR catalysis.^{28,29} During the last decade,

Functional Materials Division, CSIR-Central Electrochemical Research Institute, Karaikkudi - 630006, Tamil Nadu, India.
E-mail: duraisamyjeyakumar@gmail.com; Tel: +914565 241437 Electronic Supplementary Information (ESI) available: [Materials, characterization, Catalyst and MEA preparation, Figures S1-S9]. See DOI: 10.1039/b000000x/

nanoporous films (in the order of 100 nm thick) have been synthesized by de-alloying metal-alloy foils or galvanic replacement reaction resulting in enhanced ORR activity.^{30–35} For example, de-alloyed Pt-Ni porous film was shown to have enhanced ORR activity.³⁶ But, controlling the particle shape, pore size at nanoscale and electrode fabrication process in nanoporous films were found to be tedious, limiting their catalytic applications in fuel cells. Hence, there is a great challenge towards facile synthesis of bimetallic nanoporous structures with sizes below 10 nm which will facilitate ease cathode fabrication for effective ORR. Gao et al., have synthesized α -PtO₂ NPs and showed a better mass and specific activity than conventional Pt/C catalyst.³⁷ However, to enhance the performance they have remarked the need of a suitable carrier for loading α -PtO₂ NPs. It is envisaged that, Pt clusters will have steps and kink sites favourable for the formation of Pt (IV) species that may have enhanced ORR activity.³⁸ But unfortunately, aggregation of free standing Pt clusters makes it difficult for their practical applications. Hence, the formation of nanoporous Au-Pt NPs may be a facile and easy way to have Pt islands on Au surface towards enhanced ORR catalysis.

In this work, we have synthesized nanoporous Au_{100-x}Pt_x NPs (x = 20, 15, 10, 5) from Au_{100-x}Ag_{2x} nano-alloys (x = 20, 15, 10, 5) through galvanic replacement reaction. The porous nature of nanoporous Au-Pt NPs was predicted from surface plasmon resonance (SPR) and confirmed by low angle x-ray diffraction (LAXRD), high angle annular dark field scanning transmission electron microscopy (HAADF-STEM) and cyclic voltammetric (CV) studies. In addition, HAADF-STEM images also show the presence of porous Au and Pt islands in Au₈₅Pt₁₅ NPs. X-ray photoelectron spectroscopy (XPS) results reveal the presence of higher quantities of Pt (IV) in nanoporous Au₈₅Pt₁₅/C catalyst. Electrochemical studies of Au₈₅Pt₁₅/C catalyst shows excellent methanol tolerant ORR activity compared to other nanoporous Au-Pt/C and HiSPEC Pt/C catalysts. Furthermore, the enhanced methanol tolerant ORR activity of Au₈₅Pt₁₅ was observed from RDE studies, *ca.*, high mass activity, mass-specific activity, more positive onset potential and half wave potential for ORR along with high figure of merit (FOM). Meanwhile, the efficient and enhanced Pt utilization in nanoporous Au₈₅Pt₁₅/C catalyst has been assured by the stabilization of FOM in the presence of methanol. Preliminary full cell studies have been carried out using nanoporous Au₈₅Pt₁₅/C as the cathode material and the details are presented in this paper.

Experimental

Synthesis of Au-Ag nano-alloys

Typical synthesis procedure for the Au₈₅Ag₃₀ alloy NPs were described as follows: Same procedure were followed for the preparation of Au_{100-x}Ag_{2x} nano-alloys (x = 20, 15, 10, 5) with their appropriate precursors ratios. In a typical experiment, 7.8 mgs of HAuCl₄.3H₂O and 1.3602 mgs of AgNO₃ were taken in 100 ml water and continuously stirred for five minutes.

The reaction mixture was slightly turbid due to the formation of AgCl. In order to solubilize the AgCl, the reaction mixture was heated at 100 °C under constant stirring. As a result, turbid solution changes to a clear pale yellow solution, to which 2.5 ml of 1% trisodiumcitrate decahydrate was added as capping agent. The boiling precursors were co-reduced by adding 1ml of 0.15% NaBH₄ at a single shot and the sol colour turns light yellowish pink to brownish yellow with increasing 'x' values (x = 5 to 20) intimating the Au-Ag nano-alloy formation. The Au_{100-x}Ag_{2x} suspensions were centrifuged and utilized for optical, transmission electron microscopy (TEM), HAADF-STEM and LAXRD analysis.

Synthesis of nanoporous Au-Pt NPs from Au-Ag nanoalloys

Nanoporous Au_{100-x}Pt_x NPs were synthesized through galvanic replacement reaction from citrate capped spherical Au_{100-x}Ag_{2x} alloy NPs in aqueous medium using K₂PtCl₄ solution at ambient temperature. In a typical experiment, Au_{100-x}Ag_{2x} suspensions were treated with 'x' mole equivalent of K₂PtCl₄ and the solution was stirred for 60 m. The colour of the suspensions turns to pinkish, indicating the replacement of Ag by Pt (i.e. nanoporous Au-Pt formation) with increase in turbidity due to AgCl formation. The Au_{100-x}Pt_x suspensions were centrifuged to remove AgCl and clear supernatant solution containing the sol was used for further analysis. Details of preparation of Au_{100-x}Ag_{2x}/C and Au_{100-x}Pt_x/C materials are presented in ESI, †.

Results and discussion

Several attempts have been made to prepare Au-Ag nano-alloys in organic medium using oleylamine to avoid AgCl precipitation.^{39,40} There are few reports on the synthesis of Au-Ag nano-alloy in aqueous medium.^{41,42} In the present case, co-reduction of Au and Ag precursors were carried out in aqueous medium at 100°C to avoid the problem of AgCl precipitation. The optical absorption spectra of Au_{100-x}Ag_{2x} NPs and Au_{100-x}Pt_x NPs are presented in Fig. 1. It can be seen from the Fig. 1A that the Au_{100-x}Ag_{2x} NPs (x= 20, 15, 10, 5) shows a single SPR band (SPB) between 482 nm to 507 nm. It is pertinent to note that the SPB of 10 nm sized Ag and Au is around 415 nm and 520 nm respectively. In our case, the SPB of Au_{100-x}Ag_{2x} NPs occurs between the SPB of Au and Ag and gradually blue shifted (table 1) with increase in silver content (increase in 'x' values) confirming the Au-Ag nano-alloy formation.⁴³ The blue shift with increasing concentration of Ag is further confirmed by the SPR spectra of Au₈₅Ag₆₀ nano-alloy (ESI, Fig. S3†). In contrast, the SPB of Au_{100-x}Pt_x NPs (Fig. 1B) are slightly broadened and red shifted compared to Au_{100-x}Ag_{2x} NPs and appears between 492 nm and 516 nm indicating the replacement of Ag by Pt. It is also interesting to note that, the SPB of Au_{100-x}Pt_x nanoporous materials is also blue shifted with increasing 'x' values due to the formation of Pt islands on Au surface. If complete Pt shell is formed, then the SPB of Au_{100-x}Pt_x NPs might be diminished,⁴⁴ but the presence of SPR confirms the nanoporous nature of this material. To ascertain

the role of Pt islands in SPB blue shift, the Ag from $\text{Au}_{100-x}\text{Ag}_{2x}$ NPs was stripped using Bromine water. The SPB of this bromine etched porous Au NPs is seen at around 513 nm (ESI, Fig. S4†), which is closely similar to that of Au NPs. Hence, the existence of SPR band for all 'x' values in $\text{Au}_{100-x}\text{Pt}_x$ NPs could be attributable to exposed porous Au with Pt islands and the lack of complete Pt shell.

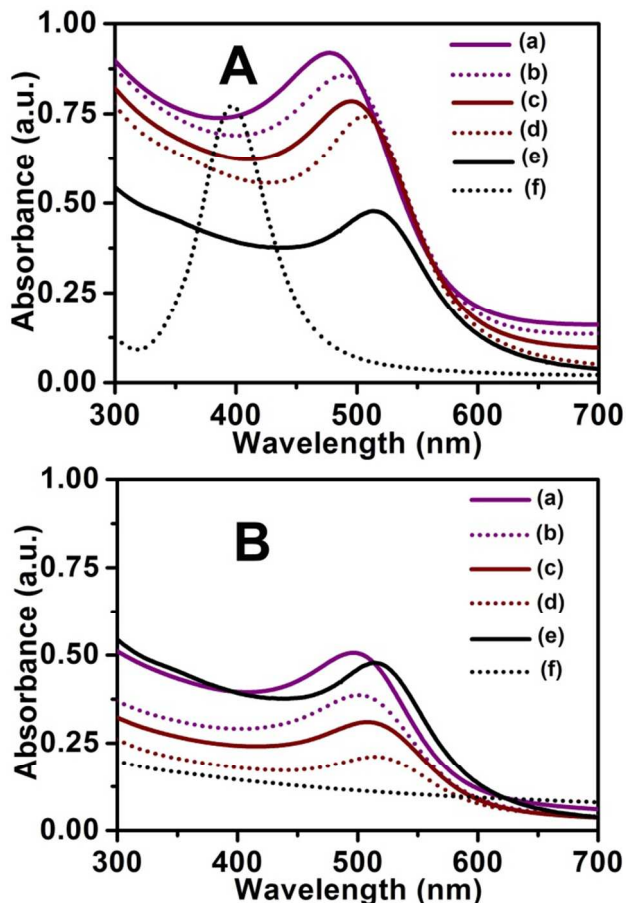


Fig. 1 (A) SPR spectra for $\text{Au}_{100-x}\text{Ag}_{2x}$ alloy NPs (a-d) $x = 20, 15, 10, 5$, (e) Au NPs, (f) Ag NPs respectively. (B) SPR spectra for nanoporous $\text{Au}_{100-x}\text{Pt}_x$ NPs (a-d) $x = 20, 15, 10, 5$, (e) Au NPs, (f) Pt NPs respectively.

Powder x-ray diffraction patterns (Fig. 2) of $\text{Au}_{100-x}\text{Ag}_{2x}/\text{C}$ and $\text{Au}_{100-x}\text{Pt}_x/\text{C}$ are compared with the standard patterns of Ag (JCPDS 04-0783), Au (JCPDS 04-0784) and Pt (JCPDS 04-0802) and found to have characteristics similar to FCC system. The lines are indexed and the lattice constant values, crystallite size (calculated using Scherrer formula) are listed in ESI, table S1†. It can be seen that the lattice constant values have decreased marginally for $\text{Au}_{100-x}\text{Ag}_{2x}$ NPs when compared to Ag NPs and Au NPs, whereas, for $\text{Au}_{100-x}\text{Pt}_x$ NPs it is shifted towards that of Pt with increase in x values. This type of behaviour has been reported for bimetallic NPs.^{27,44} Galvanic replacement reaction of a lower valent metal by a higher valent metal generally results in the formation of hollow structures.⁴⁵ In the present case, Ag in $\text{Au}_{100-x}\text{Ag}_{2x}$ nanoalloy was

galvanically replaced by Pt using K_2PtCl_4 as the reactant. It is trivial that two silver atoms are replaced by one Pt during the reaction. Hence, this may result in the formation of pores/voids in the resultant $\text{Au}_{100-x}\text{Pt}_x$ nanomaterials.

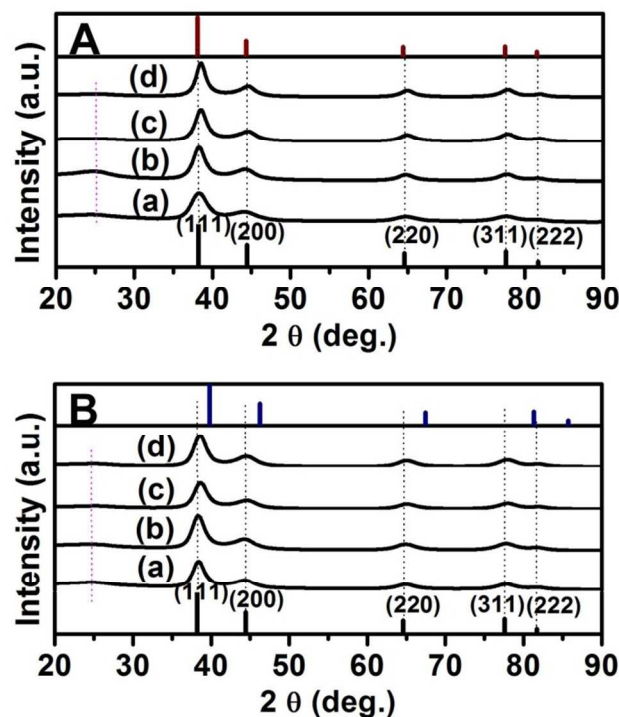


Fig. 2 (A) Powder XRD patterns of $\text{Au}_{100-x}\text{Ag}_{2x}/\text{C}$ alloys (a-d) $x = 20, 15, 10$ and 5 respectively compared with standard Au (black solid vertical line) and Ag (brown solid vertical line) patterns. (B) Powder XRD patterns of nanoporous $\text{Au}_{100-x}\text{Pt}_x/\text{C}$ nanomaterials (a-d) $x = 20, 15, 10$ and 5 respectively compared with standard Au (black solid vertical line) and Pt (blue solid vertical line) patterns.

To ascertain this, LAXRD analysis (Fig. 3) for $\text{Au}_{85}\text{Ag}_{30}$, $\text{Au}_{85}\text{Pt}_{15}$ (derived from $\text{Au}_{85}\text{Ag}_{30}$ and $\text{Au}_{85}\text{Ag}_{60}$) and $\text{Au}_{85}\text{Pt}_{20}$ were performed. There was no low angle peak for $\text{Au}_{85}\text{Ag}_{30}$ NPs indicating the material is not porous, whereas $\text{Au}_{85}\text{Pt}_{15}$ NPs clearly shows a peak at around 1.08° , which suggests the presence of nanopores (microporous) in this material. $\text{Au}_{80}\text{Pt}_{20}$ and $\text{Au}_{85}\text{Pt}_{15}$ derived from $\text{Au}_{85}\text{Ag}_{60}$ also show low angle peaks at 0.65° and 0.60° respectively indicating the increased porosity in these materials. $\text{Au}_{90}\text{Pt}_{10}$ did not show prominent low angle peak (very low intense peak at around 2.0°), whereas $\text{Au}_{95}\text{Pt}_5$ did not show any peak at low angle. This result is comparable with the LAXRD pattern of mesoporous silica and other porous materials.⁴⁶ This is further corroborated by HAADF-STEM studies of this material (*vide infra*).

XPS spectra of $\text{Au}_{85}\text{Ag}_{30}/\text{C}$ and $\text{Au}_{85}\text{Pt}_{15}/\text{C}$ NPs were deconvoluted using Gaussian-Lorentzian curve fitting⁴⁴ with chi-square value less than 2 and are presented in Fig. 4. An examination of the Fig. 4A shows one set of peaks for Au $4f_{7/2}$ and Au $4f_{5/2}$ energy levels at around 84.33 eV & 87.98 eV

attributable to metallic Au.⁴⁷ Likewise, the Fig. 4B shows two peaks at around 368.23 eV & 374.19 eV corresponding to 3d_{5/2} and 3d_{3/2} states of metallic Ag in Au₈₅Ag₃₀ alloy NPs.⁴⁷

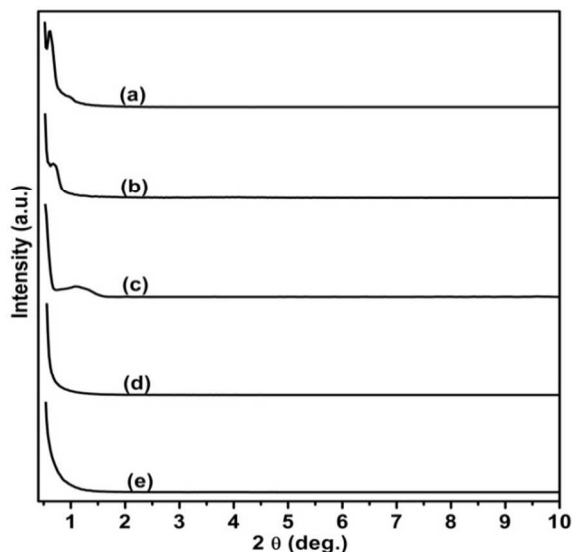


Fig. 3 Low angle XRD patterns of (a) nanoporous Au₈₅Pt₁₅ NPs derived from Au₈₅Ag₆₀ NPs., (b-d) nanoporous Au_{100-x}Pt_x (x=20, 15, 10) and (e) Au₈₅Ag₃₀ nanoalloy respectively.

Similarly, XPS of Au₈₅Pt₁₅/C NPs (Fig. 4C) shows peaks corresponding to Au and Pt energy levels. Au gives rise to two set of peaks at around 84.43 eV & 86.05 eV and 88.07 eV & 89.50 eV corresponding to Au 4f_{7/2} and 4f_{5/2} levels of Au⁰ and Au (I) respectively.⁴⁷ On the contrary, the Pt centre exhibits three sets of peaks for the energy levels of 4f_{7/2} and 4f_{5/2} at around (71.33 & 74.73 eV), (72.71 & 76.11 eV), (74.51 & 77.91 eV).⁴⁷ These peaks can be assigned for Pt⁰, Pt (II) and Pt (IV) states with the relative peak areas of 50:22.5:27.5. Generally, for Pt NPs the binding energy levels for Pt⁰ and Pt (II) were observed dominantly with trace levels of Pt (IV) (5-10% peak area). Generally, Pt clusters are expected to have more steps and kinks sites favouring Pt (IV) states.³⁸ Hence, it may be concluded that Pt in Au_{100-x}Pt_x NPs is present as isolated islands on nanoporous Au surface. Further, the trace level of Au (II) states observed in the present case is attributed to strong interaction of Pt (IV) and the underlying porous Au structure. The transmission electron microscopy (TEM) image (Fig. 5A) of Au₈₅Ag₃₀ alloy NPs shows that the particles are smooth and spherical with a size range of 6 to 8 nm. Fig. 6A depicts the TEM image of Au₈₅Pt₁₅ NPs, in which the particles are porous and spherical with a size range of 7.0 to 10.0 nm. The d - values obtained from XRD patterns and TEM- SAED patterns are consistent and the SAED intensity profiles as shown in supporting information (ESI, Fig. S5 & S6 †). The HAADF-STEM image of an Au₈₅Ag₃₀ alloy NP along with elemental mapping of Au, Ag and their line profile are presented in Fig. 5 (B-F). The HAADF-STEM image (Fig. 5B) reveals the lattice fringes. The elemental colour profile of Au and Ag (Fig. 5C &

5 D) shows random distribution and its composite mapping (Fig. 5E) indicates the mixing of Au/Ag in Au₈₅Ag₃₀ nanoalloy. The line profile (Fig. 5F) confirms and roughly mimics its ratio (i.e., 85:30 as confirmed by ICPMS). The HAADF-STEM picture of a nanoporous Au₈₅Pt₁₅ NP along with elemental mapping and line profile are presented (Fig. 6 (B-F)). The HAADF-STEM image (Fig. 6B) shows typical pattern of microporous materials with difference being the size of the particle itself in the size range of 7 nm. The elemental mapping

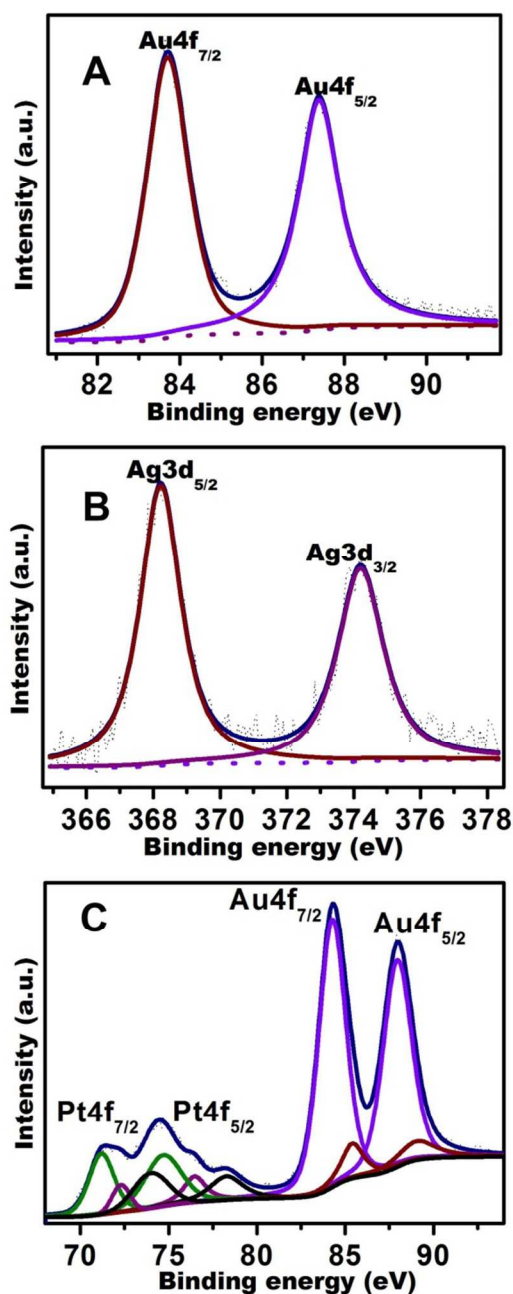


Fig. 4 (A) XPS of Au₈₅Ag₃₀/C alloy NPs showing Au 4f and (B) Ag 3d energy levels. (C) XPS of nanoporous Au₈₅Pt₁₅/C nanomaterials showing Pt 4f and Au 4f energy levels.

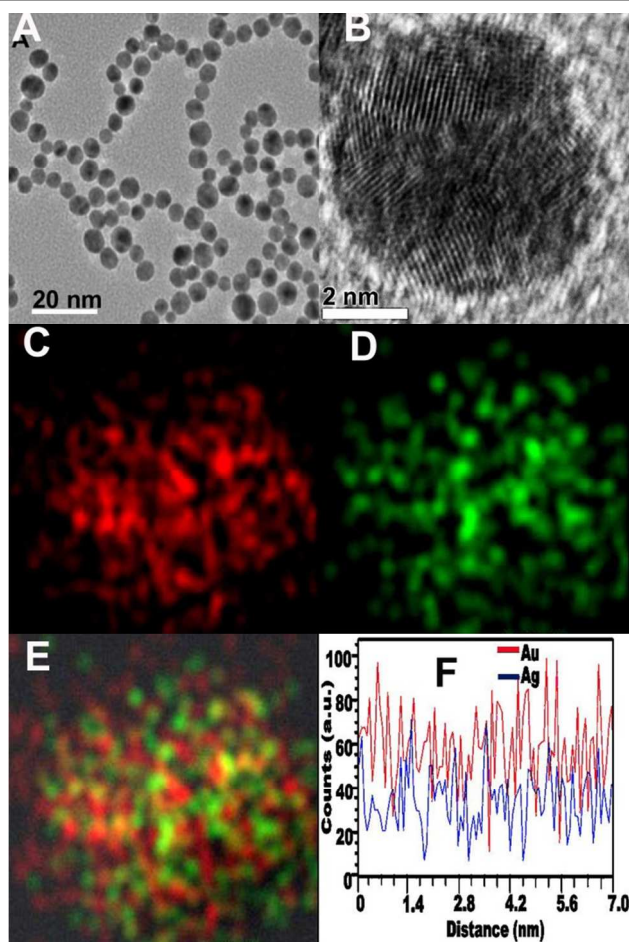


Fig. 5 (A) TEM image of $\text{Au}_{85}\text{Ag}_{30}$ alloy NPs, (B) HAADF-STEM image of a $\text{Au}_{85}\text{Ag}_{30}$ alloy NP, (C) Au elemental mapping, (D) Ag elemental mapping, (E) Au-Ag composite mapping and (F) Au-Ag line profile.

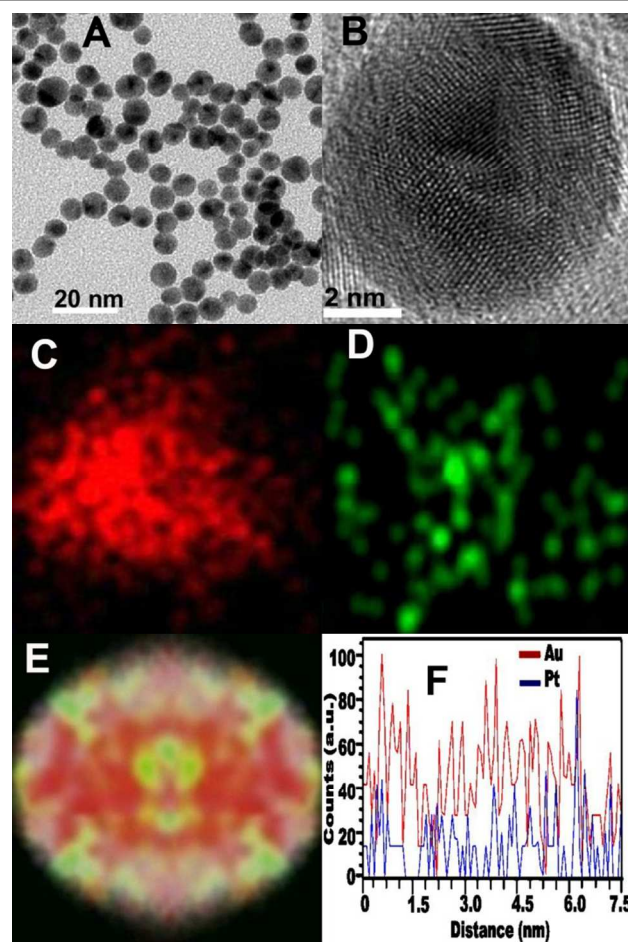


Fig. 6 (A) TEM image of nanoporous $\text{Au}_{85}\text{Pt}_{15}$ materials, (B) HAADF-STEM image of a $\text{Au}_{85}\text{Pt}_{15}$ NP, (C) Au elemental mapping, (D) Pt elemental mapping, (E) Au-Pt composite mapping and (F) Au-Pt line profile.

images of Au and Pt (Fig. 6C & 6D) shows number of voids for Au mapping and scattered Pt have been observed. In addition, the composite profile (Fig. 6E) clearly shows Pt islands and white patches all over the particle surface, indicating the presence of pores/divots.⁴⁸ Z. Liu et al., has observed this type of images with voids/divots in de-alloyed PtCo_3 material owing to the absence of Pt and Co in the elemental mapping images. In the present case, these white patches are dominant due to the nanoporous structure in $\text{Au}_{85}\text{Pt}_{15}$ NPs. The line profile (Fig. 6F) further corroborates this with consistent composition (i.e., 85:15 as confirmed by ICPMS). It is seen from Pt line that the Pt distribution drops to zero periodically, with an interval of < 0.5 nm, indicating that Pt is present as islands all over the nanoporous surface. Similarly, Au line profile also indicates that there is sharp dropping in the Au content periodically but not to zero. In addition, the absence of Ag signal in the elemental mapping images of $\text{Au}_{85}\text{Pt}_{15}$ NPs suggests the complete galvanic replacement of Ag. Both, LAXRD and HAADF-STEM studies confirms the nanoporous (microporous) nature of this material that manifests itself in the CV studies.

The stabilized CV graphs of the nanoporous $\text{Au}_{100-x}\text{Pt}_x/\text{C}$ materials ($x = 20, 15, 10, 5$) and HiSPEC Pt/C are shown in Fig. 7. During anodic cycle, the surface oxide formation of Pt and Au were seen as a wave from 1.0 V to 1.5 V and well defined surface oxide reduction peaks of Pt-O and Au-O at around 0.63 V to 1.14 V vs. RHE.⁴⁴ A closure examination of the Fig. 7 indicates that the Pt-O reduction peak current increases with increase in the 'x' values to that of Au-O reduction current. This observation indicates the increasing amount of Pt on the surface with increase in x values. The surface oxides reduction peaks can be used to calculate the ECSA and fraction of surface Au and Pt atoms from the charges under the peaks⁴⁴ for various x values and are given in table 1. The fraction of surface Pt atoms found to increase dramatically for $x = 5$ and 10 as 26.7% and 50.0 % onwards. For $x=15$ and 20 these values marginally increased as 55.5% and 57.7% respectively. These observations may be corroborated as follows: The number of atoms for 7 nm sized $\text{Au}_{100-2x}\text{Ag}_x$ nano-alloys computed using the previously reported methodology²⁹ was around 10,074 atoms with 1962 surface atoms. Depending on the x values the Au and Ag atoms

vary at the bulk and surface (ESI, Table S2†). For Au₉₅Ag₁₀ NPs, the total number of Ag atoms is 959 and the surface Ag is about 187 atoms. This means that 480 Pt atoms are required and 1755 Au surface atoms are available for nucleation and growth.

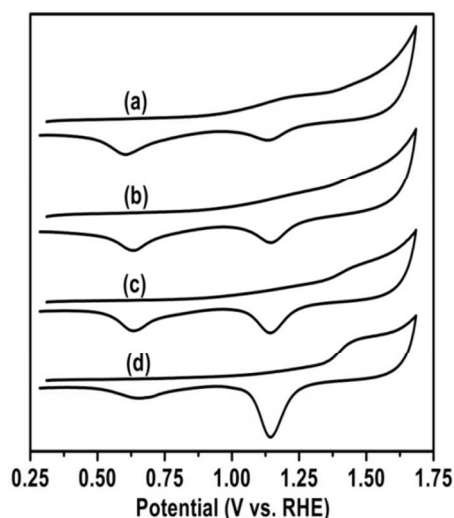


Fig. 7 CVs of nanoporous Au_{100-x}Pt_x/C catalysts (a-d) $x = 20, 15, 10, 5$ respectively coated on GC electrode in N₂ purged 1.0 N H₂SO₄ electrolyte.

This constitutes nearly 27% coverage of Pt on Au surface. Similarly for $x=10$, the value was around 57%. However, in the case of Au₈₅Ag₃₀ NPs the number of Pt atoms required to replace Ag atoms was 1314 which constitutes 90% surface coverage by Pt monolayer. During the galvanic replacement, Ag from the core leaves voids/pores in the NPs exposing fresh Au surface in the form of nanoporous structure. Hence the relative ECSA of Pt did not change dramatically for $x=15$ and 20 as mentioned earlier. To ascertain this, Au₈₅Pt₁₅ NPs derived from Au₈₅Ag₆₀ nano-alloy using Pt⁴⁺ as the precursor showed 39.5% Pt coverage. This is due to the galvanic replacement of twice the amount of Ag compared to that of Au₈₅Ag₃₀ NPs resulting in more porous material. The mechanism of nanoporous Au_{100-x}Pt_x material formation is described as follows: Generally, the galvanic replacement reaction follows nucleation growth model resulting in hollow or porous nanostructures. The standard reduction potential of [PtCl₄]²⁻/Pt (0.755 V) is higher than that of AgCl/Ag (0.22 V) and hence, the replacement of Ag by Pt²⁺ is thermodynamically feasible. Initially, the [PtCl₄]²⁻ nucleates on the Au-Ag alloy surface and oxidizes Ag to Ag⁺ which reacts with Cl⁻ forming AgCl as precipitate and gets reduced to Pt atom on the surface of Au. This process takes place sequentially adjacent to the Ag sites. By stoichiometry, for one Pt atom will replace two silver atoms from Au-Ag nanoalloy resulting in nano-hole formation. Once the surface Ag atoms are removed, Ag from the interior will also be removed. Due to Kirkendall effect, there will be a minor re-organization within the nanoparticles leading to porous structure formation. It is worthy to note that, Pt has higher surface free energy (159 meV/Å²) than Au (96.8

meV/Å²) and Ag (78 meV/Å²)⁴⁹ and hence, Pt growth would follow Volmer–Weber growth model. This would lead to the formation of Pt islands on nanoporous Au surface under galvanic replacement conditions. Moreover, the presence of SPR (Fig. 1 B) clearly shows exposed porous Au, HAADF-STEM elemental mapping images and line profile confirms porous structure with Pt islands (Fig. 6 C-F) and low angle XRD pattern (Fig. 3) shows overall nanoporous structure. The relative surface Pt fraction values of nanoporous Au_{100-x}Pt_x (ESI, Table S2†) materials also corroborate the formation of nanoporous structure. Furthermore, the characteristics of Au₈₅Pt₁₅ NPs clearly show the nanoporous nature of the material with more surface bound Pt islands that manifests in the ORR studies. Fig. 8A depicts the LSV graphs of electrochemical oxygen reduction reaction (ORR) of Au_{100-x}Pt_x/C ($x = 20, 15, 10, 5$) and HiSPEC Pt/C catalysts coated on RDE electrode at 1600 rpm in O₂ saturated H₂SO₄ electrolyte. The ORR onset and half-wave potentials were calculated from the LSV graphs and listed in (table 1). Perusal of the values indicate that, with increase in the ‘ x ’ values (up to $x = 15$) the E_{1/2} increased to more anodic values and then for $x = 20$, the value marginally decreased. Au₈₅Pt₁₅/C nanomaterial shows higher onset and half-wave potential than HiSPEC Pt/C, implying its efficacy towards ORR. Similarly, ORR studies for all the compositions at different rotation speed were carried out and the no. of electrons using Koutecky – Levich equation⁸ is described as follows:

$$\frac{1}{j} = \frac{1}{j_L} + \frac{1}{j_K} \quad (1)$$

$$\frac{1}{j} = \frac{1}{j(B \times \omega)^{1/2}} + \frac{1}{j_K} \quad (2)$$

$$B = 0.620nFC_0D_0^{3/2}\nu^{-1/6} \quad (3)$$

Where, j = measured current density, j_L = diffusion limited current density, j_K = kinetic limited current density, ω = angular velocity of RDE in rpm, n = number of electrons for ORR, F = Faraday constant, C_0 = concentration of O₂, D_0 = Diffusion coefficient of O₂ and ν = Kinematic viscosity of electrolyte. $1/j$ was plotted as a function of $\omega^{1/2}$ gave a straight line, with $1/j$ as the intercept and slope has the component of B from which the number of electrons can be calculated. It is interesting to note that all these materials reduce oxygen via 4 electron reduction process. It is pertinent to note that Au NPs shows 2e⁻ reduction process for ORR whereas Pt NPs by 4e⁻ reduction to H₂O in acidic medium. This observance of 4e⁻ reduction process for ORR ascribes to the presence of island like Pt on porous Au surface and is responsible for effective ORR activity. The ORR graphs of Au₈₅Pt₁₅/C nanomaterial at different rpm were shown in (ESI, S8†). The mass activity and mass-specific activity for ORR were calculated from the RDE studies. The mass-specific activities for nanoporous Au_{100-x}Pt_x/C materials and HiSPEC Pt/C catalysts were calculated (Fig. 8B & (table 1)) from their

steady state currents at 0.9V from RDE studies. It can be seen that Au₈₅Pt₁₅/C catalyst has higher mass-specific activity (7.8 mA) compared to HiSPEC Pt/C catalysts (2.1 mA). Likewise, the mass normalized Tafel regions were plotted for both nanoporous Au₈₅Pt₁₅/C and HiSPEC Pt/C catalysts as shown in Fig. 8C. It is noteworthy to mention that, at 0.9 V nanoporous Au₈₅Pt₁₅/C shows higher mass activity of 0.49 A/mg_{Pt} exceeding the 2017 DOE target of 0.44 A/mg_{Pt}⁵⁰ and 16 times higher than that for HiSPEC Pt/C (0.03 A/mg_{Pt}). Perusal of the data indicates that nanoporous Au₈₅Pt₁₅/C catalyst is the most efficient catalyst among the series. The enhanced mass and mass-specific activities in nanoporous Au₈₅Pt₁₅/C is ascribed to higher catalytically active Pt islands confined on nanoporous Au surface compared to HiSPEC Pt/C catalysts.

In order to understand the efficiency of Pt atom utilization, the figure of merit (FOM) for nanoporous Au₈₅Pt₁₅/C and HiSPEC Pt/C catalysts were calculated based on ORR steady state currents and surface Pt ratio according to a previously reported literature¹². The FOM of nanoporous Au₈₅Pt₁₅/C catalyst was 7.2×10^{-23} A per surface Pt atom which is higher than that for HiSPEC Pt/C catalyst (3.8×10^{-24} A per surface Pt atom) due to enhanced surface bound Pt islands in Au₈₅Pt₁₅/C as mentioned above. However, the FOM in the presence of methanol for nanoporous Au₈₅Pt₁₅/C did not suffer drastically (6.8×10^{-23} A per surface Pt atom), whereas for HiSPEC Pt/C catalyst the FOM dropped by nearly one order (4.2×10^{-25} A per surface Pt atom). The retention of FOM in nanoporous Au₈₅Pt₁₅/C catalyst not only reveals the efficacy of Pt utilization in nanoporous Au₈₅Pt₁₅/C catalyst but also ascertains its methanol tolerant ORR characteristics superior to HiSPEC Pt/C catalyst. The CVs of nanoporous Au₈₅Pt₁₅/C and HiSPEC Pt/C catalysts in the presence and absence of 0.2 M methanol are presented in Fig. 9. The lack of methanol oxidation peak at around 0.93 V (Fig. 9A) in nanoporous Au₈₅Pt₁₅/C catalyst indicates its inertness to MOR. But, HiSPEC Pt/C catalyst oxidizes methanol and prominent oxidation and reverse peaks were observed at around 0.9 V and 0.55 V vs. RHE (Fig. 9B). This is further manifested in the ORR studies. In the case of Au₈₅Pt₁₅/C catalyst (Fig. 9C) there was no major change in the ORR current profile and half-wave potential, whereas in HiSPEC Pt/C catalyst (Fig. 9D) significant changes have been observed.

Single cell studies

Membrane electrode assembly MEA was fabricated using Pt-Ru/C (0.5 mg/cm²) as anode material and nanoporous Au₈₅Pt₁₅/C (1.0 mg/cm²) as cathode material with Nafion 117 membrane as the electrolyte (ESI,†) to assess the performance. The polarization curves of the above mentioned MEA assembly are presented in Fig. 10, by feeding methanol (2M at 2 ml/min) at anode side and Oxygen (300 ml/min) at the cathode side at 40 °C, 50 °C and 60 °C. It is clearly seen from the Fig. 10 that there is no monotonous decrement in the potential as in the case

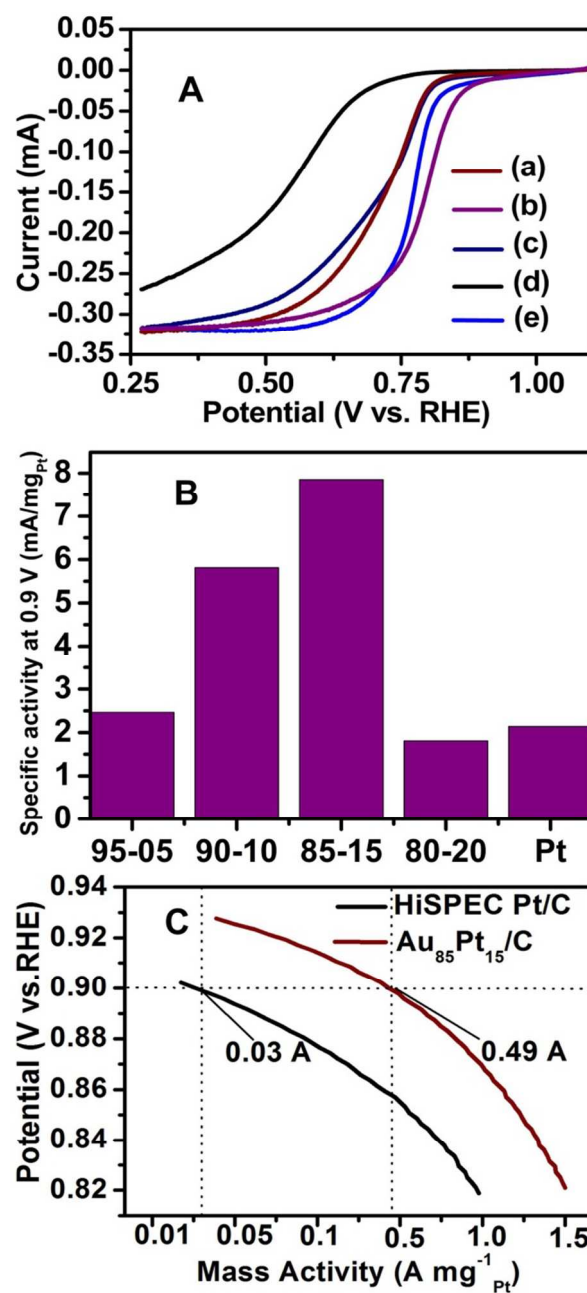


Fig. 8 (A) LSV graphs of Au_{100-x}Pt_x/C (a-d) materials at x= 20, 15, 10, 5 and (e) HiSPEC Pt/C catalysts at 1600 rpm coated on GC electrode in O₂ purged 1.0 N H₂SO₄ electrolyte (B) their respective mass specific activities at 0.9 V vs. RHE. (C) Mass normalized Tafel plot of nanoporous Au₈₅Pt₁₅/C and HiSPEC Pt/C catalysts.

of HiSPEC Pt/C catalysts, indicating the methanol tolerance ORR behaviour of nanoporous Au₈₅Pt₁₅/C as predicted from CV and RDE studies. With the increase in the temperature there is increment in the power density. It is noteworthy to mention that at 60 °C the power density was 38 mW cm⁻² but for HiSPEC Pt/C cathode catalyst the value is 16 mW cm⁻².

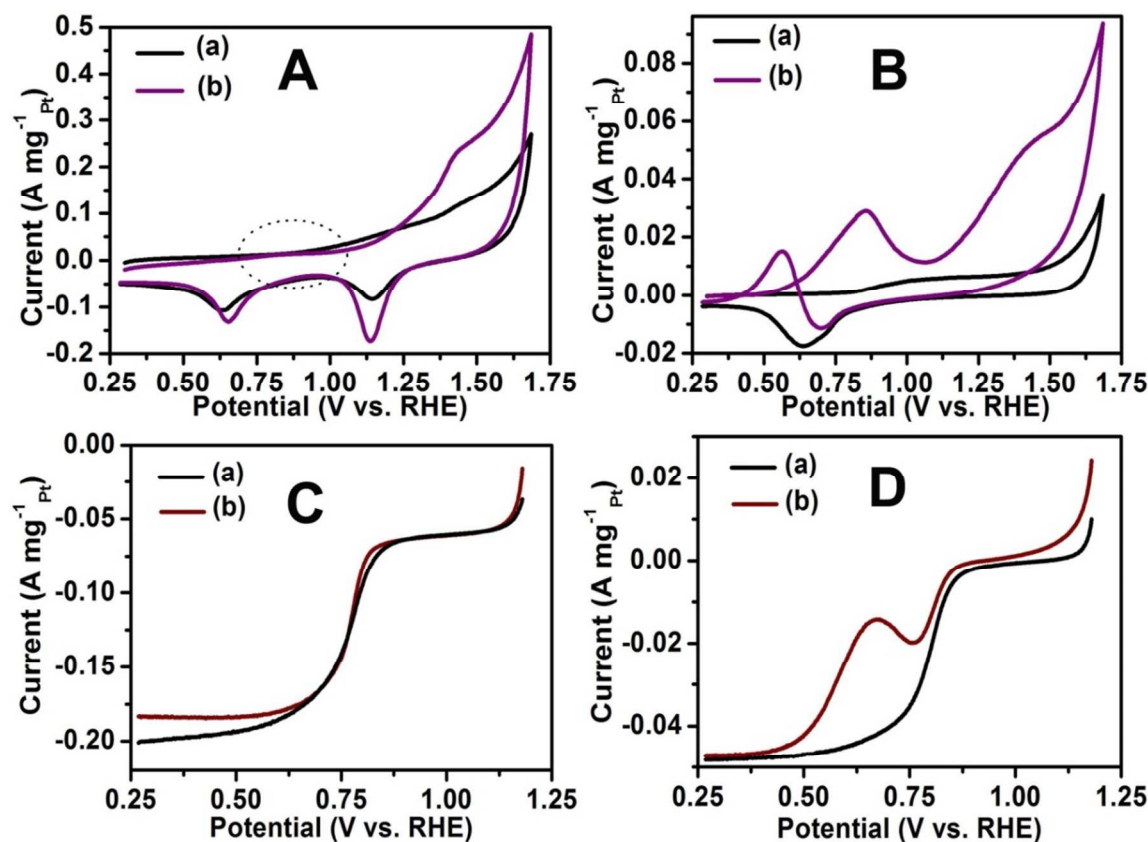


Fig. 9 (A) CVs of nanoporous Au₈₅Pt₁₅/C, (B) HiSPEC Pt/C in the absence (a) and presence (b) of 0.2 M methanol, (C) LSVs of nanoporous Au₈₅Pt₁₅/C, (D) HiSPEC Pt/C at 1600 rpm in O₂ saturated 1.0 N H₂SO₄ electrolyte in the absence (a) and presence (b) of 0.2 M methanol.

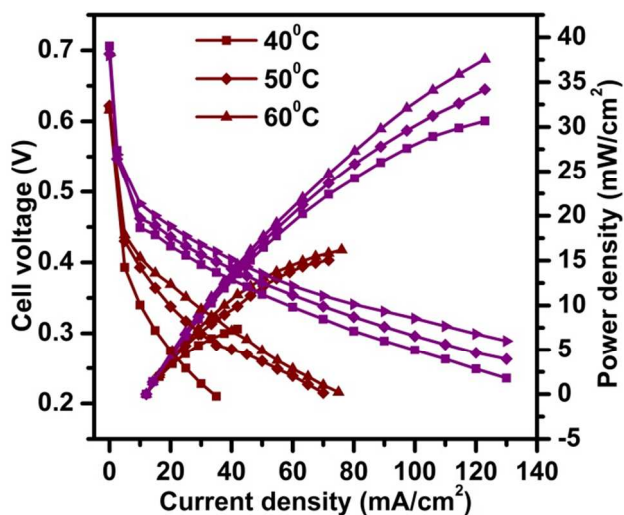


Fig. 10 Polarization curves showing the steady state performance for nanoporous Au₈₅Pt₁₅/C (purple line) cathode material compared with commercial HiSPEC Pt/C (brown line) catalysts at different temperatures.

In a recent literature, Antonino and his co-workers has reported an output of 34 mW/cm² employing Pt-Pd₃Co as the cathode material at 60 °C.⁵¹ In addition, the same cell fed with air

instead of oxygen gave the power density of 22 mW cm⁻² (ESI, S9†). Optimisation of cell parameters and studies on the stability of the nanoporous Au-Pt catalysts are in the offing.

Conclusions

To sum up, among the Au_{100-x}Pt_x nanoporous materials, Au₈₅Pt₁₅/C material was found to be an efficient electro-catalyst for ORR, with excellent attributes in terms of onset potential, half wave potential, mass activity, mass-specific activity and FOM with very good methanol tolerance, when compared to HiSPEC Pt/C commercial catalyst. The higher mass activity and specific activity of nanoporous Au₈₅Pt₁₅/C essentially arise due to the Pt islands that bound on nanoporous Au surface, leading to more Pt (IV) for enhanced ORR activity. CV studies clearly show that this material does not oxidize methanol, which may be due to the underlying porous Au structure that may not facilitate MOR. Furthermore, RDE experiments on ORR in the presence of methanol clearly indicate that the onset potential did not change significantly and the E_{1/2} value also did not suffer any shift. These properties result in minimizing the mixed cathode potential and fulfil the requisites of a suitable ORR catalyst as evidenced from full cell studies. Preliminary studies reveal that the performance of nanoporous Au₈₅Pt₁₅/C is

better than commercial Pt/C material. Further, the one pot synthetic strategy for nanoporous materials will not only help in reducing the amount of scarce and expensive Pt, but also paves a robust way out for preparing efficient ORR catalysts with other suitable nanoporous metal structures for DMFCs.

Acknowledgement

One of the authors P. A. thanks Department of Science and Technology, New Delhi for the award of DST-INSPIRE fellowship. The authors thank Director, CSIR-CECRI for his continuing support and permission to publish this work. The authors thank Central Instrumentation Facility, CSIR-CECRI for the characterization facilities, Advanced Instrumentation Research Facility, Jawaharlal Nehru University, New Delhi for the measurement of HAADF-STEM and Indian Institute of Technology-Madras, Chennai for Low Angle XRD data and National Aerospace Laboratory, Bangalore for XPS measurement. The authors thank Fuel cell division, CSIR-CECRI (Chennai unit) for their help in full cell studies. The authors also thank Dr. N. Ilayaraja and Mr. N. Prabu for their help during this work. The authors thank MULTIFUN ILP, CSIR for the financial support.

Notes and references

- X. Zhao, M. Yin, L. Ma, L. Liang, C. Liu, J. Liao, T. Lu, and W. Xing, *Energy Environ. Sci.*, 2011, **4**, 2736.
- A. S. Aricò, S. Srinivasan, and V. Antonucci, *Fuel Cells*, 2001, **1**, 133–161.
- I. E. L. Stephens, A. S. Bondarenko, U. Grønbyerg, J. Rossmeisl, and I. Chorkendorff, *Energy Environ. Sci.*, 2012, **5**, 6744.
- A. Morozan, B. Josselme, and S. Palacin, *Energy Environ. Sci.*, 2011, **4**, 1238.
- P. Hernandez-Fernandez, S. Rojas, P. Oc'ón, J. L. Fierro, and M. A. Pe'na, *J. Power Sources*, 2008, **177**, 9–16.
- G. Selvarani, S. V. Selvaganesh, S. Krishnamurthy, G. V. M. Kiruthika, P. Sridhar, S. Pitchumani, and A. K. Shukla, *J. Phys. Chem. C*, 2009, **113**, 7461–7468.
- E. Antolini, T. Lopes, and E. Gonzalez, *J. Alloys Compd.*, 2008, **461**, 253–262.
- G. Fu, K. Wu, J. Lin, Y. Tang, Y. Chen, Y. Zhou, and T. Lu, *J. Phys. Chem. C*, 2013, **117**, 9826–9834.
- W. Wang, Q. Huang, J. Liu, Z. Zou, M. Zhao, W. Vogel, and H. Yang, *J. Catal.*, 2009, **266**, 156–163.
- E. Franceschini, M. Bruno, F. Viva, H. R. Corti, and F. J. Williams, *Electrochim. Acta*, 2012, **71**, 173–180.
- Y. Wei, C. Liu, and K. Wang, *Chem. Commun.*, 2011, **47**, 11927–11929.
- J. Yang, W. Zhou, C. H. Cheng, J. Y. Lee, and Z. Liu, *ACS Appl. Mater. Interfaces*, 2010, **2**, 119–26.
- S. Ghosh, S. Mondal, and C. Retna Raj, *J. Mater. Chem. A*, 2014, **2**, 2233.
- D. Wang, P. Zhao, and Y. Li, *Sci. Rep.*, 2011, **1**, 37.
- H.-L. Jiang and Q. Xu, *J. Mater. Chem.*, 2011, **21**, 13705.
- Y. Bing, H. Liu, L. Zhang, D. Ghosh, and J. Zhang, *Chem. Soc. Rev.*, 2010, **39**, 2184–202.
- J. W. Hong, S. W. Kang, B.-S. Choi, D. Kim, S. B. Lee, and S. W. Han, *ACS Nano*, 2012, **6**, 2410–9.
- S. Chen, P. J. Ferreira, W. Sheng, N. Yabuuchi, L. F. Allard, and Y. Shao-Horn, *J. Am. Chem. Soc.*, 2008, **130**, 13818–13819.
- Z. Wen, J. Liu, and J. Li, *Adv. Mater.*, 2008, **20**, 743–747.
- C.-W. Liu, Y.-C. Wei, C.-C. Liu, and K.-W. Wang, *J. Mater. Chem.*, 2012, **22**, 4641.
- L. Chen, L. Kuai, and B. Geng, *CrystEngComm*, 2013, **15**, 2133.
- S. Guo, Y. Fang, S. Dong, and E. Wang, *J. Phys. Chem. C*, 2007, **111**, 17104–17109.
- F. Ye, H. Liu, W. Hu, J. Zhong, Y. Chen, H. Cao, and J. Yang, *Dalt. Trans.*, 2012, **41**, 2898–2903.
- G.-R. Zhang, D. Zhao, Y.-Y. Feng, B. Zhang, D. S. Su, G. Liu, and B.-Q. Xu, *ACS Nano*, 2012, **6**, 2226–36.
- F. Lima, J. Zhang, M. Shao, K. Sasaki, M. B. Vukmirovic, E. A. Ticianelli, and R. R. Adzic, *J. Phys. Chem. C*, 2007, **111**, 404–410.
- J. Yang, X. Chen, X. Yang, and J. Ying, *Energy Environ. Sci.*, 2012, **5**, 8976.
- L. Leppert, R. Q. Albuquerque, A. S. Foster, and S. Kümmel, *J. Phys. Chem. C*, 2013, **117**, 17268–17273.
- F. Zheng, W. Wong, and K. Yung, *Nano Res.*, 2014, **7**, 410–417.
- B. Du, O. Zaluzhna, and Y. J. Tong, *Phys. Chem. Chem. Phys.*, 2011, **13**, 11568–74.
- H. M. Chen, R.-S. Liu, M.-Y. Lo, S.-C. Chang, L.-D. Tsai, Y.-M. Peng, and J.-F. Lee, *J. Phys. Chem. C*, 2008, **112**, 7522–7526.
- G. Zhang, S. Sun, M. Cai, Y. Zhang, R. Li, and X. Sun, *Sci. Rep.*, 2013, **3**, 1526.
- S. Guo, S. Dong, and E. Wang, *J. Phys. Chem. C*, 2009, **113**, 5485–5492.
- C. Xu, R. Wang, M. Chen, Y. Zhang, and Y. Ding, *Phys. Chem. Chem. Phys.*, 2010, **12**, 239–46.
- M. Wang, W. Zhang, J. Wang, A. Minett, V. Lo, H. Liu, and J. Chen, *J. Mater. Chem. A*, 2013, **1**, 2391.
- C. Xu, Y. Liu, Q. Hao, and H. Duan, *J. Mater. Chem. A*, 2013, **1**, 13542.
- R. Wang, C. Xu, X. Bi, and Y. Ding, *Energy Environ. Sci.*, 2012, **5**, 5281.
- M. Gao, Z. Lin, J. Jiang, C. Cui, Y. Zheng, and S. Yu, *J. chem. EUR*, 2012, **18**, 8423–8429.
- A. Arico, A. Shukla, H. Kim, S. Park, M. Min, and V. Antonucci, *Appl. Surf. Sci.*, 2001, **172**, 33–40.
- L. Sun, W. Luan, and Y. J. Shan, *Nanoscale Res. Lett.*, 2012, **7**, 225.
- C. Wang, H. Yin, R. Chan, and S. Sun, *Chem. Mater. Commun.*, 2009, **21**, 2007–2009.
- W.-J. Kim, S. Kim, A. R. Kim, and D. J. Yoo, *Ind. Eng. Chem. Res.*, 2013, **52**, 7282–7288.
- E. Csapó, A. Oszkó, E. Varga, Á. Juhász, N. Buzás, L. Kőrösi, A. Majzik, and I. Dékány, *Colloids Surfaces A Physicochem. Eng. Asp.*, 2012, **415**, 281–287.
- S. Liu, G. Chen, P. N. Prasad, and M. T. Swihart, *Chem. Mater.*, 2011, **23**, 4098–4101.
- N. Ilayaraja, N. Prabu, N. Lakshminarasimhan, P. Murugan, and D. Jeyakumar, *J. Mater. Chem. A*, 2013, **1**, 4048.

45. V. Bansal, H. Jani, J. Du Plessis, P. J. Coloe, and S. K. Bhargava, *Adv. Mater.*, 2008, **20**, 717–723.
46. Y. Kim, J. G. Kang, S. Lim, and J. H. Song, *J. bull.korean chem. Soc.*, 2005, **26**, 1129–1131.
47. and C. J. P. Alexander V. Naumkin, Anna Kraut-Vass, Stephen W. Gaarenstroom, *Mater. Meas. Lab.*, 2012.
48. Z. Liu, H. Xin, Z. Yu, Y. Zhu, J. Zhang, J. A. Mundy, D. A. Muller, and F. T. Wagner, *J. Electrochem. Soc.*, 2012, **159**, F554–F559.
49. R. J. Needs and M. Mansfield, *J. Phys. Condens. Matter*, 1989, **1**, 7555–7563.
50. U.S Department Of Energy, *Off. energy Effic. Renew. energy*, 2005.
51. A. S. Aricò, A. Stassi, C. D'Urso, D. Sebastián, and V. Baglio, *Chem. A Eur. J.*, 2014, **20**, 1–7.

Figure of Contents

$\text{Au}_{85}\text{Pt}_{15}/\text{C}$ nanoporous material with surface Pt islands synthesized by galvanic replacement reaction (GRR), act as efficient methanol-tolerant ORR catalyst with high figure of merit, mass and specific activities performed well in full cell studies.

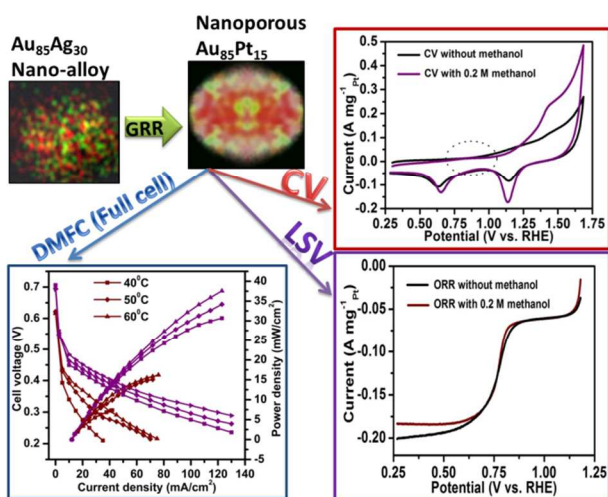


Table 1: Spectral and electrochemical data on Au_{100-x}Ag_x and Au_{100-x}Pt_x nano-materials

x	Au _{100-x} Ag _{2x}		Au _{100-x} Pt _x					
	SPR (nm)	SPR (nm)	Onset (V)	E _{1/2} (V)	Relative ECSA		Mass activity (A mg ⁻¹ of Pt)	Mass-specific activity (mA/mg _{Pt} @0.9 V)
					Au	Pt		
5	507	516	0.85	0.54	0.73	0.27	0.493	2.4
10	501	510	1.03	0.70	0.49	0.51	0.523	5.8
15	491	501	1.06	0.78	0.43	0.57	0.491	7.8
20	482	492	1.05	0.71	0.41	0.59	0.083	1.8
Au ₈₅ Ag ₆₀	476		--	--	--	--	--	--
Au ₈₅ Pt ₁₅ *	--	489	--	--	0.36	0.64	--	--
HiSPEC Pt/C	--	--	1.05	0.79	--	1.00	0.032	2.1

Potentials are with reference to RHE

*Prepared from Au₈₅Ag₆₀ nanoalloy using Pt⁴⁺ as the galvanic replacing species